# ADVANCES IN THE DEVELOPMENT AND VALIDATION OF CFD-BWR, A TWO-PHASE COMPUTATIONAL FLUID DYNAMICS MODEL FOR THE SIMULATION OF FLOW AND HEAT TRANSFER IN BOILING WATER REACTORS

**Adrian Tentner[1], Simon Lo[2], David Pointer[1], Andrew Splawski[2]**

*1 - Argonne National Laboratory, Argonne, Illinois, USA*
*2 - CD-adapco, London, UK*

## Abstract

This paper presents an overview of the model development and validation of an advanced Computational Fluid Dynamics (CFD) computer code (CFD-BWR) that allows the detailed analysis of two-phase flow and heat transfer phenomena in Boiling Water Reactor (BWR) fuel bundles. The CFD-BWR code is being developed as a customized module built on the foundation of the commercial CFD-code STAR-CD which provides general two-phase flow modeling capabilities. The model development strategy that has been adopted by the development team for the prediction of boiling flow regimes in a BWR fuel bundle includes the use of local flow topology maps and topology-specific phenomenological models specifically designed for a 3-dimensional CFD code. The paper reviews the key boiling phenomenological models and focuses on several key experiment analyses for the validation of two-phase BWR phenomena models including flow regime experiments, cladding-to-coolant heat transfer and Critical Heat Flux experiments, and the BWR Full-size Assembly Boiling Test (BFBT).

## 1. INTRODUCTION

An effort to develop and validate an advanced Computational Fluid Dynamics (CFD) model, CFD-BWR, which allows the detailed analysis of the two-phase flow and heat transfer phenomena in Boiling Water Reactor (BWR) fuel assemblies under various operating conditions has been underway in recent years. The CFD-BWR code uses an Eulerian Two-Phase approach and is also referred to as the E2P modeling framework. It is being developed as a customized module built on the foundation of the commercial CFD-code STAR-CD which provides general two-phase flow modeling capabilities. We described in [1-3] the model development strategy that has been adopted by the development team for the prediction of boiling flow regimes in a BWR fuel bundle. The model validation strategy and results of experiment analyses focused on individual two-phase phenomena as well as integral system behavior have been presented in [4,5].

The paper reviews the two-phase models implemented in the CFD-BWR code, and emphasizes the modeling of inter-phase and coolant-cladding momentum and energy exchanges. The boiling model used in the BFBT analyses is the second generation of the CFD-BWR model, which includes a local flow topology map that allows the cell-by-cell selection of the local flow topology [6]. Local flow topologies can range from a bubbly flow topology where the continuous phase is liquid, to a transition flow topology, to a droplet flow topology where the continuous phase is vapor, depending primarily on the local void fraction. Results of three experiment simulations using these models are presented, including: a) Flow regime experiment analyses, b) Wall heat transfer and Critical Heat Flux experiment analyses, and c) BWR full bundle experiment analyses.

## 2. EULERIAN TWO-PHASE BOILING CFD MODEL

### 2.1 Methodology

The model development strategy that has been adopted by the development team for the simulation of boiling flow phenomena in a BWR fuel bundle was described in [2]. A central concept is that of a local inter-phase surface topology map which determines the local flow configuration as a function of flow conditions and prescribes which models and properties are relevant for each computational cell. The E2P Boiling model uses an inter-phase surface topology map that includes a bubbly topology, a droplet or mist topology and a transition topology. This topology map is described in more detail below. The inter-phase surface topology map is used to determine the local configuration of the vapor and liquid phases as a function of local flow conditions and prescribes which models and properties are relevant for each computational cell. The ensemble of many computational cells with relatively simple inter-phase surface topologies can provide complex global topologies that include all the traditional sub-channel flow regimes, as shown in [6].

The direct simulation of individual bubbles or the transition from bubbly flow, through slug and churn flow, to annular flow is not currently within our scope for practical reasons. To resolve individual small bubbles or large bubbles of size comparable to channel diameter would consume large computer resources on the necessarily fine grids and short timescales, and above all on the extraction of suitable time-averaged results from the simulation of a chaotic process. Instead, we use a representative bubble diameter dependent on the local conditions for each cell. For transition-topology cells we use a topology-based combination of the terms appropriate for the basic topologies, bubbly and mist. This can be interpreted as having a transition topology cell where a fraction of the cell volume presents the bubbly topology while the remaining volume presents the mist topology. An alternative interpretation is that the map is prescribing the probability of being in one topology or the other while solving equations for the time-averaged flow. This approach is illustrated in more detail below.

### 2.2 Transport Equations

The STAR-CD Eulerian two-phase solver tracks the mass, momentum, and energy of the liquid and vapor phases in each computational cell. Full details of the Eulerian two-phase flow models in STAR-CD and discussion of prior academic and commercial two-phase experience can be found in [7, 8]. The main equations solved are the conservation of mass, momentum and energy for each phase.

The conservation of mass equation for phase $k$ is:

$$\frac{\partial}{\partial t}(\alpha_k \rho_k) + \nabla.(\alpha_k \rho_k u_k) = \dot{m}_{ki} - \dot{m}_{ik} \qquad (1)$$

The conservation of momentum equation for phase k is:

$$\frac{\partial}{\partial t}(\alpha_k \rho_k u_k) + \nabla.(\alpha_k \rho_k u_k u_k) - \nabla.\left(\alpha_k \left(\tau_k + \tau_k^t\right)\right) = -\alpha_k \nabla p + \alpha_k \rho_k g + M \qquad (2)$$

The conservation of energy equation for phase k is:

$$\frac{\partial}{\partial t}(\alpha_k \rho_k e_k) + \nabla.(\alpha_k \rho_k u_k e_k) - \nabla.(\alpha_k \lambda_k \nabla T_k) = Q \qquad (3)$$

An extended $k-\varepsilon$ model containing extra source terms that arise from the inter-phase forces present in the momentum equations is used to model turbulence in the flow [7].

### 2.3 The boiling model

The inter-phase heat and mass transfer models were obtained by considering the heat transfers from the gas and the liquid to the gas/liquid interface, see Fig. 1. The net heat transfer to the interface is used to compute the mass transfer rate between the two phases. The heat transfer rate from the liquid to the interface is:

$$\dot{q}_l = h_l A_d \left(T_l - T_{sat}\right) \tag{4}$$

The heat transfer rate from the gas to the interface is:

$$\dot{q}_g = h_g A_d \left(T_g - T_{sat}\right) \tag{5}$$

Assuming that all the heat transferred to the interface is used in mass transfer (i.e. evaporation or condensation), the mass transfer rate can be written as:

$$\dot{m} = \frac{\dot{q}_l + \dot{q}_g}{h_{fg}} \tag{6}$$

A model describing the heat transfer between the heated wall and the coolant has also been developed. The heat flux from the wall is divided into three parts according to a wall heat partitioning model which includes convective heat for the liquid, evaporative heat for generation of steam and quench heat for heating of liquid in the nucleation sites. The details of the boiling model and the wall heat partitioning model can be found in [2, 8].

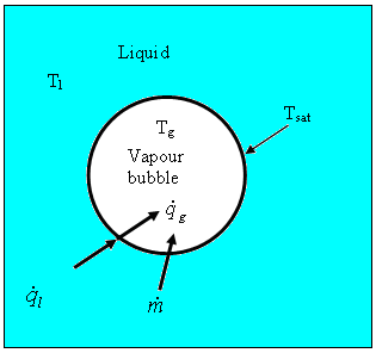


Figure 1 Heat and mass transfer between a vapor bubble and liquid

### 2.4 Inter-phase Surface Topology Map and Local Flow Configuration

Inter-phase interactions in multiphase fluids depend on both the area and the topology of interface. Sub-channel thermal-hydraulic codes rely on flow regime maps to evaluate the interface topology using cross-section-averaged flow parameters. CFD codes, which divide the flow space into much finer computational cells cannot rely on the traditional sub-channel flow regimes, but must evaluate instead the local inter-phase surface topology. The ensemble of many computational cells with relatively simple inter-phase surface topologies can provide complex global topologies that include all the traditional sub-

channel flow regimes, as illustrated in Figure 2. We have shown in [6] that results of CFD simulations of upward boiling flow experiments lead to sub-channel flow regimes in agreement with the established Hewitt and Roberts flow regime map [9].

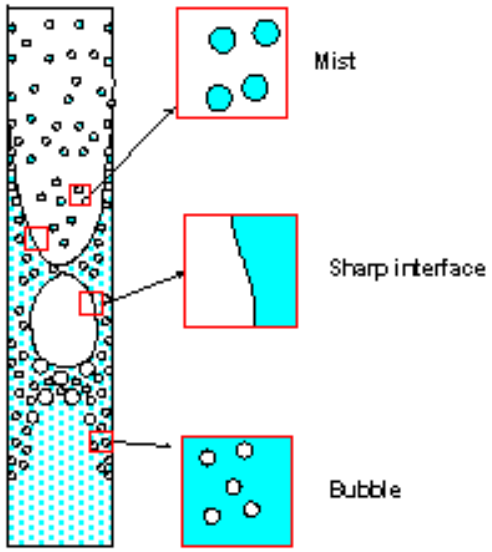


Figure 2 Schematic view of upward boiling flow in a channel with heated walls and selected cell topologies

Most of the advanced CFD codes currently allow the simulation of dispersed flows only (bubbly or mist flows) where the topology is originally defined. The E2P boiling model uses a locally calculated topology variable to allow the following topologies: a) a bubbly flow topology with spherical vapor bubbles in a continuous liquid, b) a droplet or mist topology with spherical liquid droplets flowing in a continuous vapor field, and c) a transition topology which combines the features of the two previous topologies in various proportions. The local topology is determined in this model using a local topology map based on the local void fraction. This 1-dimensional topology map is illustrated in Fig. 3 together with the associated flow topologies.

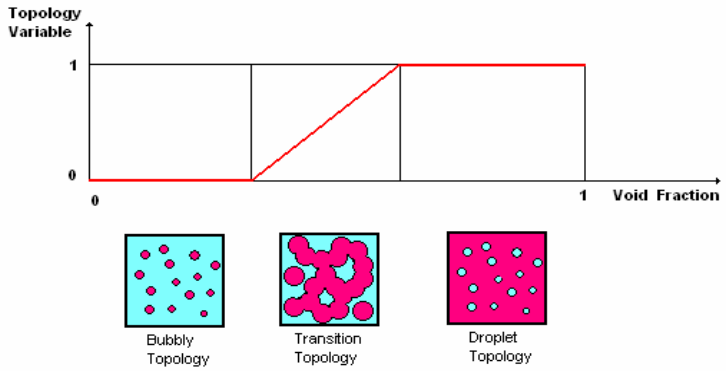


Figure 3 Inter-Phase Surface Topology Map used for the 2nd Generation Boiling Model.

This topology map does not address directly the presence of cells that contain a sharp single-connected interface, such as wall cells that contain a thin liquid film. To address this problem, the second generation

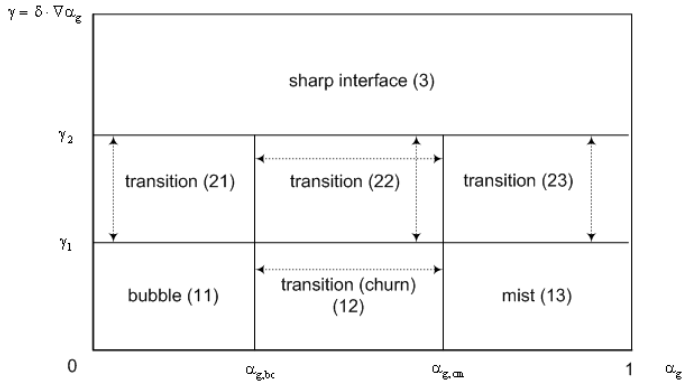


Figure 4 Extended inter-phase surface topology map.

E2P model has introduced an extended two-dimensional local inter-phase surface topology map [3] illustrated in Figure 4. According to this map, the inter-phase surface topology in each mesh cell is determined by two quantities, i.e. void fraction $\alpha_g$ and void fraction difference $\gamma = \delta \cdot \left| \nabla \alpha_g \right|$, at distances of about the characteristic mesh size $\delta = \min\left\{ \Delta_x, \Delta_y, \Delta_z \right\}$.

This extended inter-phase surface topology map is currently used only for near-wall cells. Wall cells that satisfy specific conditions that include both the local void fraction and the void fraction difference are treated in the E2P boiling model as a special liquid film topology case. Inter-phase mass, momentum, and energy transfer models have been developed for the two-phase flow topologies illustrated in Fig. 3 and calculations for the verification and validation of these models are discussed below. As demonstrated in [6], the use of the local inter-phase surface topology map allows the modelling of complex sub-channel scale topologies that emerge from combinations of many computational cells with one of the topologies shown in Figure 3. E.g., the typical sub-channel annular flow regime could be resolved into a distinct core flow region in which the gas phase is continuous and the local mist topology is used, separated by transition topology cells from a liquid film on the wall where the local bubbly topology is used.

## 2.5 Two-phase Heat, Mass and Momentum Exchange Models

The inter-phase heat and mass transfer models were obtained by considering the heat transfers from the vapor and the liquid to the vapor/liquid interface [1]. Assuming that the net heat transferred to the interface is used in mass transfer (i.e. evaporation or condensation), the inter-phase mass transfer rate can be calculated as a function of the heat transfer rates from the vapor and the liquid to the interface as well as the latent heat of vaporization. The local inter-phase surface topology is determined using the topology map discussed above, and is then used to determine the appropriate vapor and liquid heat transfer coefficients and inter-phase surface area. Since bubble or droplet populations rather than individual bubbles or droplets are followed in this method, the energy and mass exchange are applied to a characteristic bubble or droplet which would represent the ensemble average of all bubbles or droplets within a given cell. A mixture of large Taylor bubbles and small bubbles is assumed to exist in the slug-flow transition topology which is used to determine the local heat transfer coefficients and inter-phase surface area.

A model describing the heat transfer between the heated wall and the coolant has also been developed [1, 8]. The heat flux from the wall is divided into three parts according to a wall heat partitioning model which includes convective heat for the liquid, evaporative heat for generation of steam and quench heat

for heating of liquid in the nucleation sites. If the wall heat flux is specified, rather than the wall temperature, this model allows the calculation of the wall temperature that corresponds to the specified heat flux. If the flow analysis is coupled with neutronics, the temperatures of the fuel pin and cladding must be determined together with the coolant temperatures as a conjugate heat transfer problem. Heat transfer within the solids is described by a separate equation, which is solved together with the coolant energy equation to obtain the temperature at the solid/fluid interface. When this wall temperature is greater than the saturation temperature, the boiling model described above is applied on the fluid side to produce vapor. Vapor condensation on walls with a temperature below the saturation temperature is also considered.

The inter-phase and wall forces considered in the model are: drag, turbulent dispersion, virtual mass, lift, and wall lubrication forces. In addition, inter-phase momentum transfer is associated with mass transfer, hence the total force applied to phase i, which may be in contact with phase k and/or a channel wall, is expressed as:

$$F = F_D + F_{TD} + F_{VM} + F_L + F_{WL} + \dot{m}_{ki} u_i - \dot{m}_{ik} u_k \tag{7}$$

The second generation E2P boiling model has extended the treatment of the inter-phase forces to cover the spectrum of flow topologies expected in a BWR fuel assembly. The force models cover vapor bubbles in the sub-cooled or saturated bubbly flow topology, a mixture of Taylor bubbles and smaller bubbles in the slug-flow transition topology, and liquid droplets in the droplet or mist topology. Details of the treatment of inter-phase drag can be found in [3, 7, and 8].

## 3. TWO-PHASE FLOW MODEL VALIDATION

Rigorous validation efforts during the model development phase have focused on numerous two-phase flow experiments focused on separate boiling effects. The location of vapor generation onset or film dry-out onset, axial temperature profile and axial and radial void distributions were calculated and compared with experimental data. Reasonable agreement between computed results and measured data was obtained in these analyses [2, 3, and 5]. In this paper we review results of three experiment analyses that were used to validate important capabilities of the CFD-BWR model: a) Flow regime experiment analyses, b) Wall heat transfer and Critical Heat Flux experiment analyses, c) BWR full bundle experiment analyses.

### 3.1 Flow Regime Experiment Analyses

The ability of the CFD-BWR code to reproduce the experimentally observed flow regimes of upward vapor-water flow in vertical tubes have been verified in analyses of experiments performed by Bennett et. al. described in Ref. [10]. These experiments recorded the flow regimes of a water-vapor mixture flowing in a vertical circular column with diameter 0.127 m at pressures ranging from 3.45 to 6.9 MPa, The flow regimes were observed at an instrumented observation section of the circular pipe. We used the flow regime map of Hewitt and Roberts, introduced in Ref. [9] to establish the correspondence between the CFD calculated results and the traditional sub-channel flow regimes. The borders of the flow regime map proposed by Hewitt and Roberts using the coordinates $\chi_l = \rho_l \cdot (\alpha_l W_l)^2$ and $\chi_g = \rho_g \cdot (\alpha_g W_g)^2$ are shown in Fig. 5. As shown in Ref. [9], the map describes well the observations of the experiments performed by Bennett et al.

The CFD simulations of the upward pipe flow assumed to be axis-symmetric were performed in a quasi-steady-state mode, for each set of specified initial conditions, and were stopped when the specified convergence condition was satisfied. The calculated flow conditions at the observation station, at $z$=1.5 m from inlet, were used to determine: a) the coordinates of the corresponding point in the flow regime map and the corresponding flow regime predicted by the map, and b) the flow regime determined by the calculated void fraction distribution at the observation station and a fixed set of rules describing the accepted flow regime topology.

In the calculations, the channel inlet conditions were specified to cover the flow regime map uniformly. For each set of inlet conditions the coordinates of the corresponding point in the flow regime map presented in Fig. 5 were determined at the observation section at $z$=1.5 m from inlet by integration over the channel section:

$$\chi_i = \rho_i \cdot \left( \frac{1}{S} \cdot \int \alpha_i W_i dS \right)^2, \tag{8}$$

where $\rho_i$ is density of phase $i$, $\alpha_i$ is the volume fraction of phase $i$ ($\alpha_g + \alpha_l = 1$), $S$ is sectional area at $z$=const, and $W_i$ is axial velocity for phase $i$.

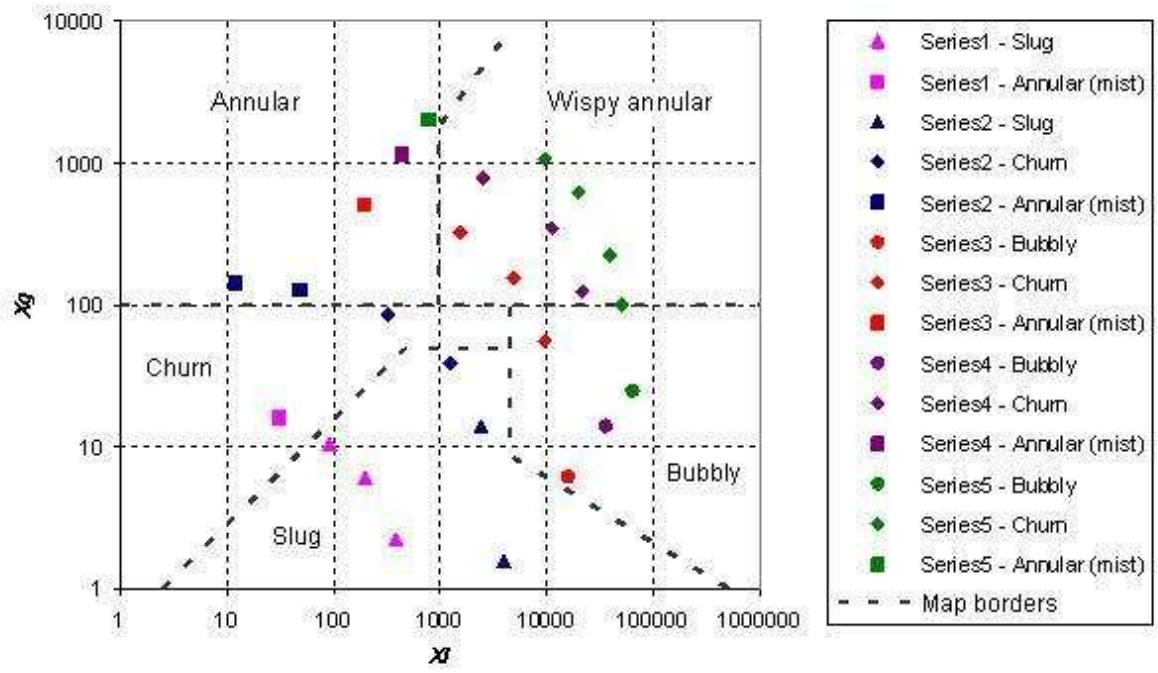


Figure 5 Calculated flow regimes on the original Hewitt and Roberts flow regime map

The flow regime corresponding to each case studied is determined by the map position, determined in turn by the coordinates calculated with Equation 8. Various cases studied are shown by markers in the flow regime map presented in Fig. 5. The flow regime for each case was also determined using the calculated void fraction radial distributions at the observation station and a set of topology criteria. The computed flow regime symbols, based on calculated void fraction topology features, are explained in the legend. It is noted that the flow regime determination from visual or calculated data using topology features can be quite subjective. To ensure consistency, a fixed set of criteria have been used to determine

the flow regime corresponding to the calculated radial void fraction distribution. The physical characteristics for each flow regime were identified by Hewitt and Roberts in Ref. [9] and the corresponding criteria used to determine the flow regimes in our analysis were described in Ref. [6].

The flow regime results plotted in Fig. 5 show that the calculated bubbly and slug flow regimes fit well into the experimental flow regime bounds defined by the Hewitt and Roberts flow regime map. As discussed in Ref. [6] the separation of the churn and wispy annular regimes is quite artificial, and in more recent flow regime maps the churn and wispy annular regimes are not separated [11]. Thus, we did not separate the calculated churn and wispy annular regimes, which are represented by the same symbol in Fig. 5. If the churn and wispy annular flow regimes are not distinguished, then the calculated churn flow regime fits well in the combined churn and wispy annular flow regime areas on the Hewitt and Roberts flow regime map.

### 3.2 Critical Heat Flux Experiment Analyses

The cladding-to-coolant heat transfer is described by a wall heat partitioning model which, used in conjunction with various local flow topologies that range from bubbly to droplet to film flow, allows the prediction of a wide range of cladding-to-coolant heat transfer regimes, including the onset of Critical Heat Flux (CHF), without the use of empirical correlations traditionally used in sub-channel codes [12]. Results of two analyses of experiments that have measured the axial distribution of wall temperature in two-phase upward flow in a vertical channel with a heated wall are presented, illustrating the ability of the cladding-to-coolant heat transfer model to capture the onset of CHF.

To validate the wall heat transfer models included in the CFD-BWR code we analyzed the static dryout experiments conducted by Becker, et al. [13, 14]. The experimental setup and results used in this paper are based on the description given by Hoyer [15]. These experiments were designed to study CHF and post-dryout heat transfer in vertical circular pipes. The loop consisted of a 7 m long test section, a condenser, feed water and main recirculation pumps, flow measuring devices and a preheater. Subcooled water was fed at the bottom of the test section. The wall was heated uniformly and all typical to BWR flow regimes were produced in the upward water/steam flow. In the experiments the outer wall temperature was measured, and the inner wall temperature has been calculated assuming an adiabatic boundary condition. The experimental data are presented as axial distributions of the inner wall temperature.

Analyses of two experiments involving flow in a vertical channel 0.01 m in diameter and 7 m in length with a uniformly heated wall were used as verification cases. Pressure in both experiments was 7.01 MPa. The experiments differed in inlet mass flux $G$ (497 kg/(s·m$^2$) and 1495 kg/(s·m$^2$)) and wall heat flux (350000 W/m$^2$ and 797000 W/m$^2$).

The calculated void fraction distributions are shown for the two experiments analyzed in Figs. 6a and 7a, respectively, with the test section shown horizontally. The characteristic flow regimes in a pipe with heated walls are simulated. Since the experiments were focused on the dryout and post dryout heat-transfer, the bubbly flow regime was not practically produced, but the slug, annular-mist and mist flow regimes were clearly observed, as well as liquid film on the wall. The calculated wall temperature is also shown in these figures, illustrating the fact that the sharp rise in the wall temperature coincides with the disappearance of the calculated liquid film in both cases.

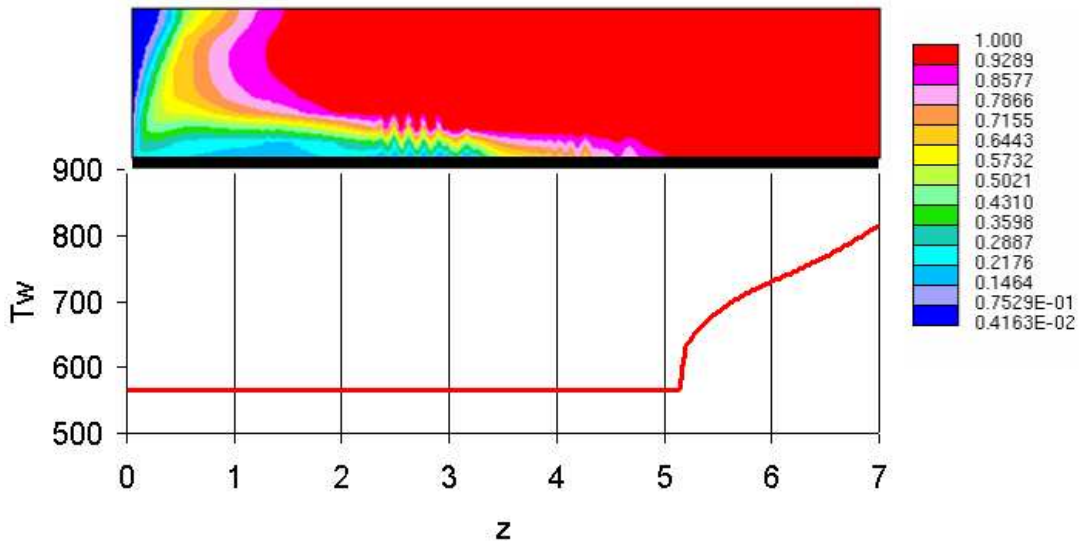


Figure 6a Calculation 1: Void fraction distribution and wall temperature

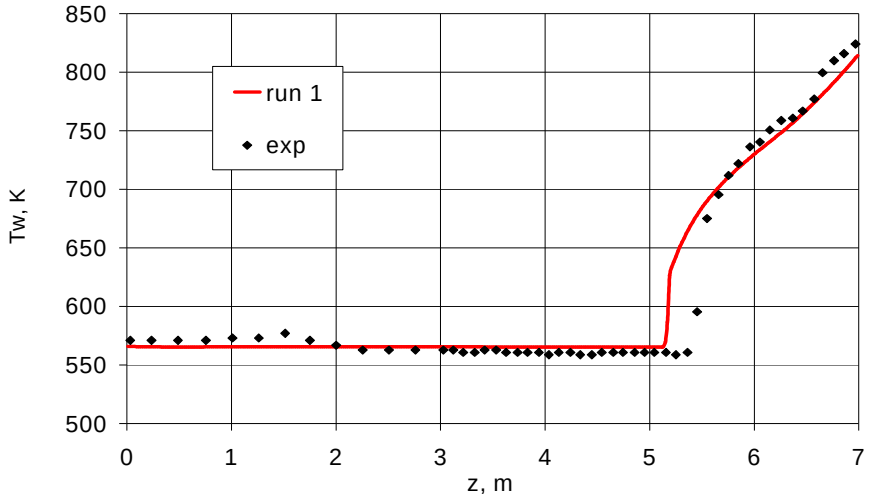


Figure 6b Wall temperature: experiment and calculation 1

In the simulation of the first experiment two wavy film regions are clearly noticeable (Fig. 6a). These waves are unlikely to be a numerical effect, since: a) the peak-to-peak distance is about 7-10 times the longitudinal cell size, b) the waves do not disappear with mesh refinement, and c) the waves are steady, i.e. they do not change noticeably with the number of iterations. There are no film waves in the second calculation (Fig.7a), which was performed in the same manner but at higher heat flux and higher inlet mass flux.

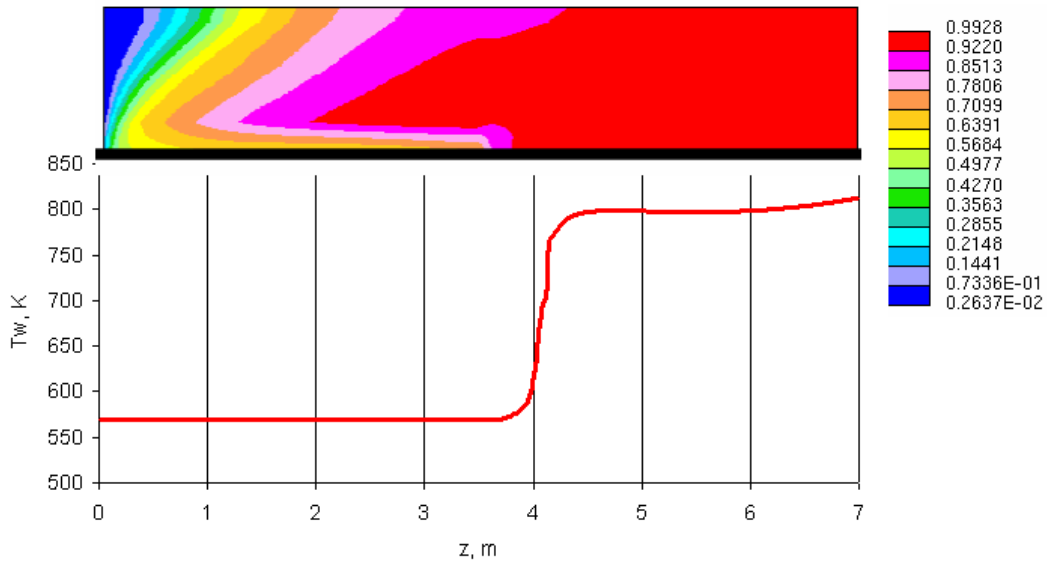


Figure 7a Calculation 2: Void fraction distribution and wall temperature

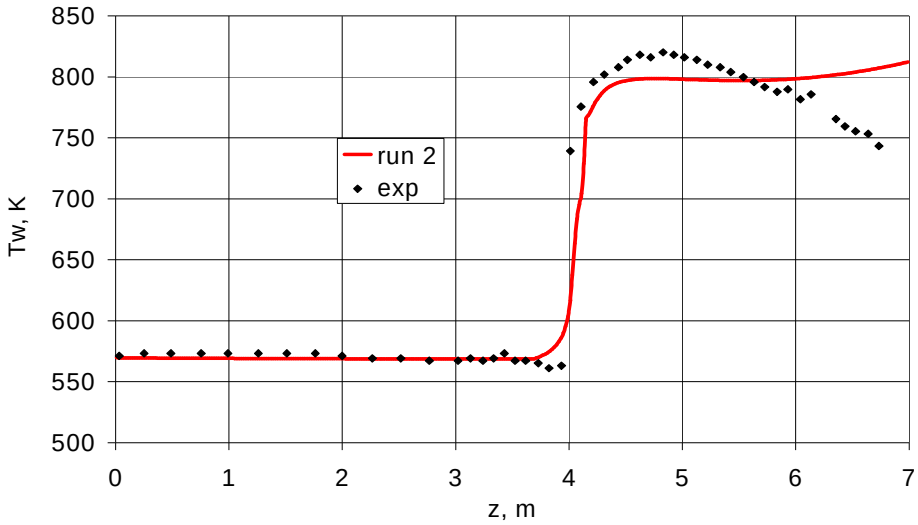


Figure 7b Wall temperature: experiment and calculation 2

The calculated wall temperature for the two experiments analyzed is compared with the corresponding measured temperature in Figs. 6b and 7b respectively. The dryout location is close to experimental data for both experiments. As for the post-dryout heat-transfer, there is rather good agreement between computed and measured wall temperatures in the first experiment, as illustrated in Fig.6b. In the second experiment, the calculated wall temperature peak is near the outlet, while the experimental temperature peak is near the dryout location, after which wall temperature decreases (Fig.7b). According to Hoyer [15], the wall temperature non-monotony is caused by evaporation of water droplets in superheated steam after the dryout elevation. This evaporation makes steam mass and, therefore, its velocity, rapidly increase. In its turn, this increases wall-steam heat transfer coefficient and decreases wall temperature.

Another potential reason for the post-dryout wall temperature decrease in the presence of many droplets is the direct heat transfer from the wall due to the impinging droplets. This heat transfer mechanism was not modeled in the analyses described above.

The comparisons of calculated wall temperatures with the corresponding measured temperatures show that the cladding-to-coolant heat transfer model implemented allows the prediction of a wide range of cladding-to-coolant heat transfer regimes, including the onset of Critical Heat Flux (CHF), without the use of empirical correlations traditionally used in sub-channel codes. Future work will enhance the cladding-to-coolant heat transfer model to include models of droplet dynamics and droplet interactions with the liquid film and the walls.

### 3.3 BWR Full Bundle Experiment Analyses

A central component of the integral model validation is the analysis of the OECD-NEA/US-NRC Benchmark based on NUPEC BWR Full-size Fine-mesh Bundle Tests (BFBT) [16]. The benchmark, begun in 2004, aimed to assess current computational capabilities for the prediction of detailed void distributions within BWR fuel assemblies. The benchmark is based on experiments, completed by NUPEC using an electrically-heated full-size model of a BWR assembly, that are sufficiently well-instrumented to provide a basis for validation of such detailed void distribution predictions. Three cases have been selected as validation problems for two-phase CFD models by the benchmark program. In these three cases, the benchmark geometry consists of 60 electrically heated pins organized in an 8 by 8 array. The electrically heated pins use the same cladding materials as BWR fuel pins and match typical BWR dimensions. The test assembly includes a large circular water channel which displaces the 4 rods at the center of the assembly. Seven ferrule spacer grids with perimeter vanes are found at uniform axial positions to both restrict the motion and deformation of the pins and introduce turbulence mixing into the flow field. The external boundary of the test section geometry is representative of a standard square BWR assembly can and is assumed to be well insulated.

All cases identified for the CFD benchmark exercise use a flat axial power profile and the radial profile shown in Figure 8. The selected cases have an inlet subcooling of 50.2 kJ/kg, an outlet pressure of 7.2 MPa, and a pin bundle inlet velocity of approximately 2.33 m/s. Variations in exit quality were achieved in the experiments considered by controlling the total current supplied to the test section. Three different exit qualities – 5, 12, and 25 percent – are considered in these analyses. For each of these cases, both macro-scale sub-channel averaged void fractions and micro-scale CT-scan void fraction distribution data are available for validation of the two-phase boiling model performance. The BFBT computational model is a finite volume model using a conformal mesh built from a combination of hexahedral and prismatic computational elements to describe the geometry of the test section. The baseline model used in the analyses described in this paper contains approximately 1.3 million cells, with 95 axial layers and 13924 cells in each axial plane, as shown in Figure 9. The model includes a simplified representation of all 7 spacer grids, as shown in Figure 10.

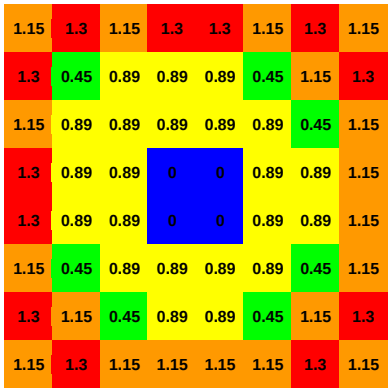


**Figure 8. Radial Pin Power Distribution Used in BFBT CFD Benchmark Cases.**

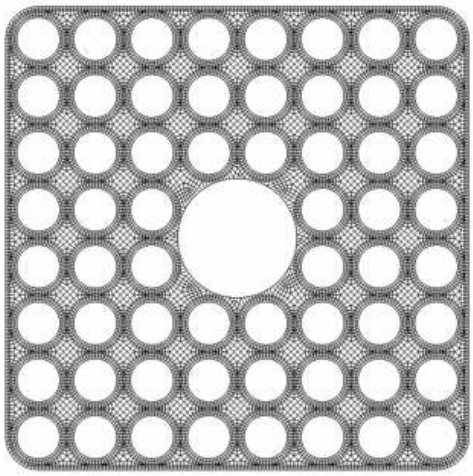

**Figure 9. Radial distribution of computational cells in each axial layer of baseline block-structured computational mesh.**

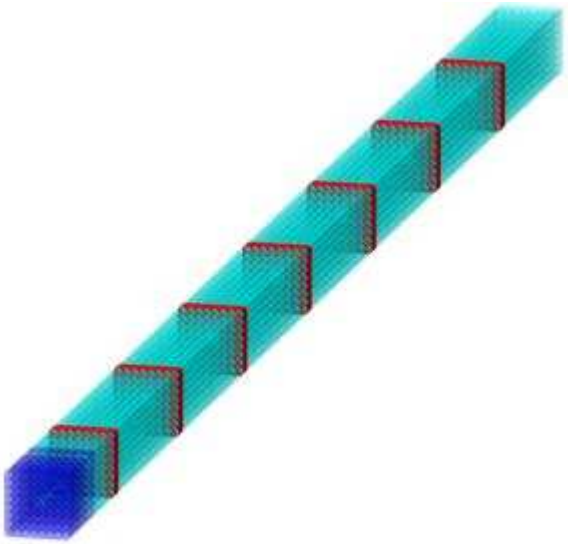

(a)

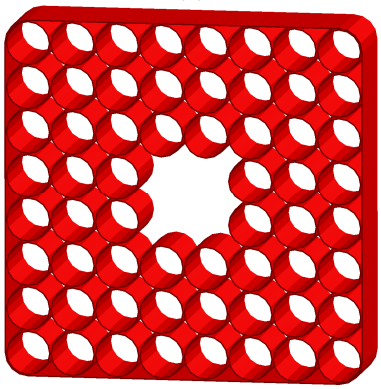

(b)

**Figure 10. (a) Illustration of the arrangement of heated pins and spacer grids in the BFBT test section, and (b) simplified spacer grid.**

Baseline case simulations previously described in [17] were performed using the baseline computational mesh as well as all default settings for user defined coefficients and parameters required by the E2P model, e.g., bubble/droplet diameters and lift coefficient. The wall lubrication and turbulent dispersal components of the momentum transfer function were not activated in these simulations. Predicted void fraction distributions at the measurement plane are shown for the high exit quality case in Figure 11, together with the corresponding measured void fraction distributions. The detailed calculated void distributions are generally in good agreement with the detailed observed void distributions capturing the formation of liquid films on the fuel pins, water channel, and assembly walls, as well as the formation of a high void fraction central region in the sub-channels. However, the predicted void fraction tends to be higher than the observed value in the corner channels, and the predicted liquid film tends to be thicker than the observed liquid film in the larger sub-channels adjacent to the water channel.

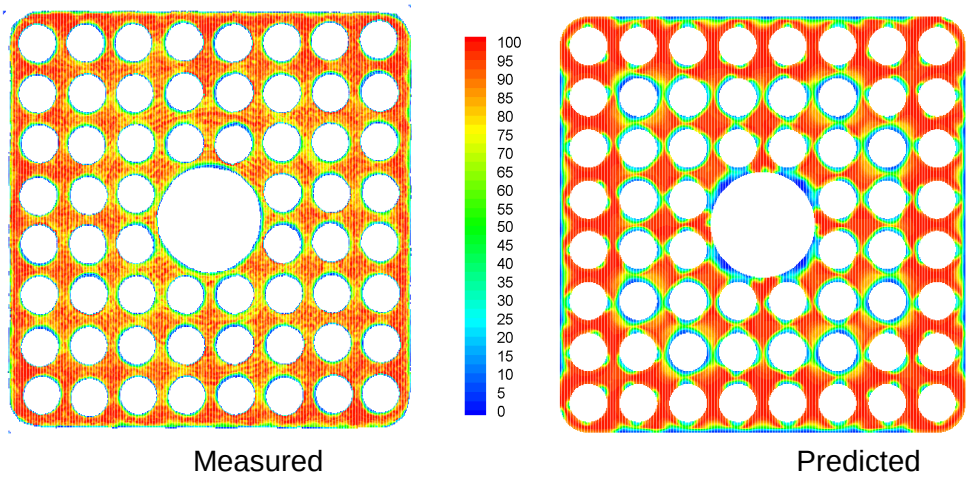


**Figure 11. Measured and predicted detailed void fraction (%) distribution at the measurement plane for the high exit quality case (25%), baseline simulation results.**

The predicted sub-channel average void fractions for all three cases are compared with the corresponding measured values in Figure 12, where the error is defined as:

$$E\,[\%] = \alpha_{s,\,calculated} - \alpha_{s,\,measured} \qquad (9)$$

where:
$\alpha_{s,\,calculated}$ = Average sub-channel calculated void fraction [%]
$\alpha_{s,\,measured}$ = Average sub-channel measured void fraction [%]

The location of the sub-channels referred to in Figure 12 is shown schematically in Figure 13. Agreement is particularly good for the highest exit quality case, and predicted sub-channel averages are within 5 - 15% of measured values for the majority of sub-channels in all cases. However, errors are particularly high in the corner sub-channels A, H, and L, where the simulation tends to over-predict the observed void fraction, and near the water channel boundary, e.g. sub-channels D and E, where the simulation tends to under-predict the observed void fraction. We showed in [18] that the higher errors in these regions are partially attributable to the increased importance of the neglected forces in these regions. The detailed void distributions calculated after the inclusion of the wall lubrication and turbulent dispersal forces indicate that the effect of these forces is to decrease the amount of vapor in the corner channels and also decrease the thickness of the liquid film on the water channel and assembly walls. These trends tend to bring the predicted detailed void distributions closer to the observed results in the sub-channels where larger errors were present in the base case, as illustrated in Figures 14 and 15 for the medium exit quality BFBT case results.

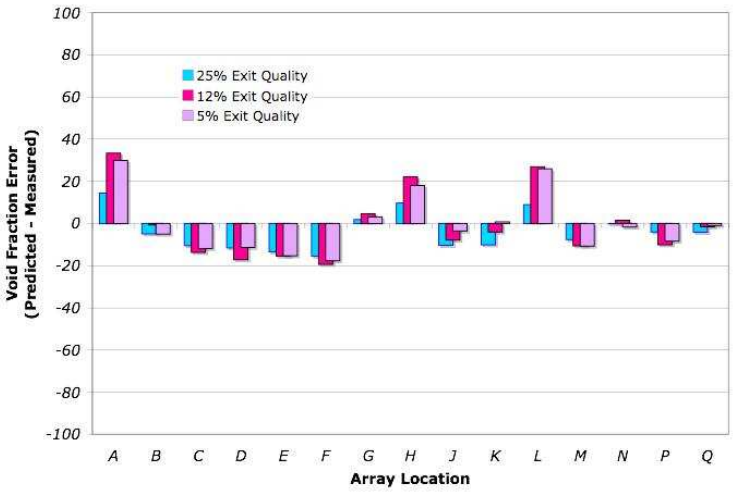


Figure 12 Sub-channel average void fraction errors for selected sub-channels, all three cases

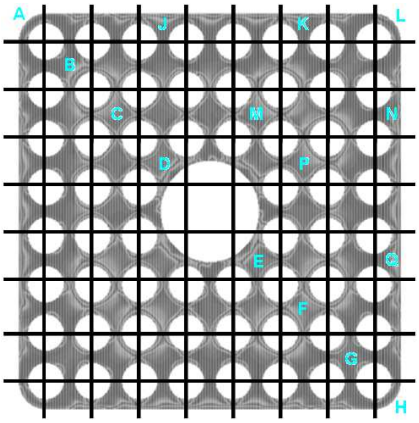


Figure 13 Sub-channels studied in the void fraction error analysis

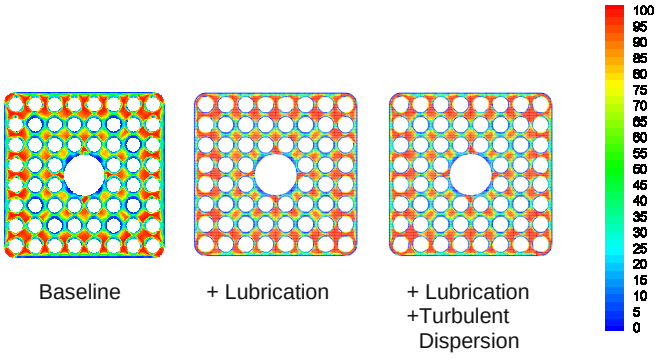


**Figure 14. Void fraction s*imulation results BFBT Test 4101-58, Exit Quality = 12%***

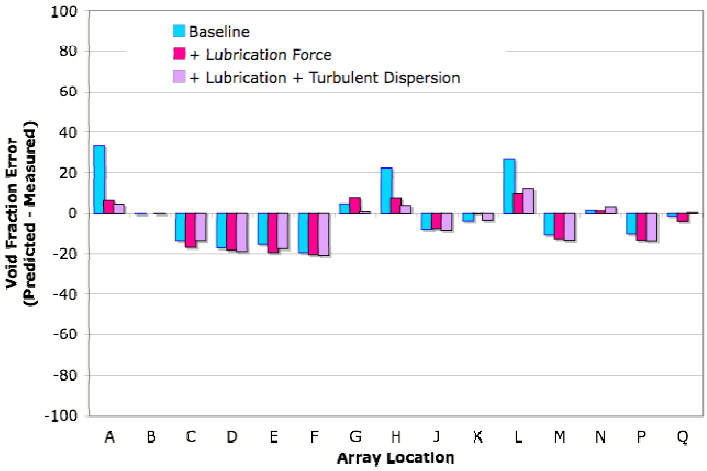


**Figure 15. Sub-channel average void fraction errors for selected sub-channels, BFBT Test 4101-58, Exit Quality = 12%**

## CONCLUSIONS

An Eulerian 2-phase boiling model has been developed for computational fluid dynamics simulations of two-phase flow phenomena in BWR fuel assemblies. The use of local inter-phase surface topologies in conjunction with a local inter-phase surface topology map allows the modeling of complex sub-channel flow regimes using a small number of basic local topologies defined for each computational cell. The extensive validation effort includes analyses of numerous two-phase flow experiments focused on separate boiling effects as well as integral fuel assembly boiling flow phenomena.

The validation of the local flow topology models has focused on the analysis of two-phase flow experiments in which flow regimes of the two-phase mixture have been observed. The detailed void distribution and local flow topologies obtained from simulations at the observation station have been aggregated to obtain calculated flow regimes, which have been compared with the flow regime map based on experimental observations. Reasonably good agreement between the computed flow regimes and the experimental flow regime map was obtained. Future work will enhance the thin-film models and expand the current local inter-phase surface topology approach to include inter-phase surface transport.

The validation of the wall-to-coolant heat transfer models has been illustrated by results of analyses of two experiments involving upward boiling water flow and dryout in a heated circular channel were presented. Comparisons of the calculated wall temperatures with the corresponding measured values show that the cladding-to-coolant heat transfer model implemented allows the prediction of a wide range of cladding-to-coolant heat transfer regimes, including the onset of Critical Heat Flux (CHF), without the use of empirical correlations traditionally used in sub-channel codes. Future work will enhance the cladding-to-coolant heat transfer model to include models of droplet dynamics and droplet interactions with the liquid film and the walls.

The integral validation of the boiling flow models has focused on the comparison of predicted void fraction distributions with experimental data in the framework of the international benchmark based on the NUPEC BFBT experiments. The void fraction distribution results presented provide a rather accurate picture of the detailed void fraction distribution in the BFBT measuring plane, capturing the formation of liquid films on the fuel pins, water channel, and assembly walls, and the formation of high void fraction central regions in the sub-channels. Future model development work will focused on enhancing the link between the local inter-phase surface topology calculations, sub-channel geometry and sub-channel flow regimes. This can be particularly relevant for the analysis of BFBT fuel assemblies, where multiple sub-channels with significantly different geometry are present.

## ACKNOWLEDGMENTS

Partial support for the development of the CFD-BWR model and the E2P boiling modeling framework has been provided by U.S. DOE-IPP, U.S. DOE-NE, and EPRI. Some of the validation results were obtained in collaboration with researchers from VNIIEF and SarovLabs in Sarov, Russia. The contributions of Drs. Andrey Ioilev, Maskhud Samigulin, and Vasily Ustinenko are particularly acknowledged.

## NOMENCLATURE

Latin

| | |
|---|---|
| $A$ | interfacial area, $m^2$ |
| $A_i$ | specific interfacial area, $m^{-1}$ |
| $C_p$ | specific heat |
| $D$ | diameter of bubbles or droplets, m |
| $e$ | enthalpy, J/kg |
| $g$ | gravitational acceleration, 9.806 $m/s^2$ |
| $h$ | heat transfer coefficient, $W/(m^2 K)$ |
| $h_{fg}$ | latent heat, J/kg |
| $\dot{m}$ | mass transfer rate, $kg/m^3$ |
| $M$ | sum of the inter-phase forces, $N/m^3$ |
| $p$ | pressure, Pa |
| $S$ | sectional area, m |
| $Q$ | inter-phase heat transfer, $W/m^3$ |
| $T$ | temperature, K |
| $T_{sat}$ | saturation temperature, K |
| $u$ | velocity vector components, m/s |
| $W$ | axial velocity component, m/s |
| $z$ | distance from inlet, m |

Greek

| | |
|---|---|
| $\alpha$ | volume fraction |
| $\gamma$ | void fraction differential |
| $\Delta_x, \Delta_y, \Delta_z$ | numerical mesh size in *x*, *y* and *z* direction |
| $\delta$ | characteristic numerical mesh size |
| $\lambda$ | thermal conductivity, W/(m·K) |
| $\mu$ | viscosity coefficient |
| $\theta$ | topology variable |
| $\rho$ | density, $kg/m^3$ |
| $\sigma_{ten}$ | surface tension coefficient, N/m |
| $\tau$ , $\tau^t$ | laminar and turbulence shear stresses, $N/m^2$ |

Subscripts

| | |
|---|---|
| $b$ | bubble (dispersed phase) |
| $d$ | droplet (dispersed phase) |
| $g$ | gas |
| $i, k$ | phase number |
| $l$ | liquid |
| $sat$ | saturation |

## REFERENCES


1. Tentner A, et al. “Development and Validation of an Extended Two-Phase Computational Fluid Dynamics Model for the Analysis of Boiling Flow in Reactor Fuel Assemblies,” Proceedings of ICAPP 2007, Nice, France, May 13-18, 2007, Paper 7483.
2. Tentner A, Lo S, Ioilev A, Samigulim M, Ustinenko V, "Computational Fluid Dynamics Modeling of Two-phase Flow in a Boiling Water Reactor Fuel Assembly", Proceedings of the International Conference on Mathematics and Computations, American Nuclear Society, Avignon, France, Sept. 2005.
3. Tentner A, et al. “Advances In Computational Fluid Dynamics Modeling Of Two Phase Flow In A Boiling Water Reactor Fuel Assembly,” Proceedings of ICONE14, the 14th International Conference on Nuclear Engineering, Miami, FL, USA, July 17-20, 2006, ICONE14-89158 (2006).
4. Pointer W. D., et al., “Eulerian Two-Phase Computational Fluid Dynamics for Boiling Water Reactor Core Analysis,” Joint International Topical Meeting on Mathematics & Computation and Supercomputing in Nuclear Applications (M&C + SNA 2007), Monterey, California, April 15-19, 2007.
5. Ustinenko V., et al., “Validation Of CFD-BWR, A New Two-Phase Computational Fluid Dynamics Model For Boiling Water Reactor Analysis,” Proceedings of CFD4NRS: OECD/NEA International & International Atomic Energy Agency (IAEA) Workshop on Benchmarking of CFD Codes for Application to Nuclear Reactor Safety, Garching, Munich, Germany, 5 - 7 September (2006).
6. Tentner A., et al. "Computational Fluid Dynamics Modeling of Two-Phase Flow and Inter-Phase Surface Topologies in a BWR Fuel Assembly," Proceedings of ICONE16, the 16th International Conference on Nuclear Engineering, Orlando, FL, USA, May 11-15, 2008.
7. STAR-CD Version 3.20 Methodology Manual, Chapter 13, CD-adapco, UK (2004).
8. Lo S., “Modeling multiphase flow with an Eulerian approach,” von Karman Institute Lecture Series - Industrial Two-Phase Flow CFD, May 23-27, von Karman Institute, Belgium (2005).
9. G..F.Hewitt, D,N,Roberts, "Study of Two-Phase Flow Patterns by simultaneous X-ray and flash photography", Atomic Energy Research Establishment Harwell, AERE-M 2159, February 1969.
10. A.Bennett, G..Hewitt, H.Kearsey, R.Keeys, P.Lacey, "Flow Visualization Studies of Boiling at High Pressure", Proc. Inst. Mech. Eng. 1965, Vol 180, Pt.3C, p.260-270
11. B.J.Azzopardi, E.Wren. “What is entrainment in vertical two-phase churn flow?” Int. J. Multiphase Flow, 2004, Vol.30, p. 89-103.
12. A. Ioilev, M. Samigulin, V. Ustinenko, P. Kucherova, A. Tentner, S. Lo, A. Splawski “Advances in the modeling of cladding heat transfer and critical heat flux in boiling water reactor fuel assemblies”, Proc. 12th International Topical Meeting on Nuclear Reactor Thermal Hydraulics (NURETH-12), Pittsburgh, Pennsylvania, USA, September 30-October 4, 2007
13. K.M.Becker, C.H.Ling, S.Hedberg, G.Strand, An experimental investigation of post dryout heat transfer. Department of Nuclear Reactor Engineering, Royal Institute of Technology, KTH-NEL-33, Sweden, 1983
14. K.M.Becker, P.Askeljung, S.Hedberg, B.Soderquist, U.Kahlbom, An experimental investigation of the influence of axial heat flux distibutions on post dryout heat transfer for flow of water in vertical tubes. Department of Nuclear Reactor Engineering, Royal Institute of Technology, KTH-NEL-54, Sweden, 1992
15. N.Hoyer, Calculation of dryout and post-dryout heat transfer for tube geometry. *Int. J. Multiphase Flow*, 1998, Vol.24, No.2. p.316-334
16. Neykov B., et al., OECD-NEA/US-NRC/NUPEC BWR Full-size Fine-mesh Bundle Test (BFBT) Benchmark, Volume I: Specifications, NEA No. 6212, NEA/NSC/DOC(2005)5, August 2006.
17. Pointer W.D., et al., "Prediction of Boiling Water Reactor Assembly Void Distributions Using a Two-Phase Computational Fluid Dynamics Model", Proceedings of ICONE16, the 16th International Conference on Nuclear Engineering, FL, USA, May 11-15, 2008.
18 Tentner A. et al, Development and Validation of a Computational Fluid Dynamics Model for the Simulation of Two-Phase Flow Phenomena in a Boiling Water Reactor Fuel Assembly, Proc. of the 17th International Conf on Nuclear Eng. ICONE17, Brussels, Belgium, July 2009